

Unsupervised motion segmentation in one go: Smooth long-term model over a video

Etienne Meunier and Patrick Bouthemy

Inria, Centre Rennes - Bretagne Atlantique, France

January 30, 2024

Abstract

Human beings have the ability to continuously analyze a video and immediately extract the main motion components. Motion segmentation methods based on deep learning often proceed frame by frame. We want to go beyond this paradigm, and perform the motion segmentation in series of flow fields of any length, up to the complete video sequence. It will be a prominent added value for downstream computer vision tasks, and could provide a pretext criterion for unsupervised video representation learning. In this perspective, we propose a novel long-term spatio-temporal model operating in a totally unsupervised way. It takes as input the volume of consecutive optical flow (OF) fields, and delivers a volume of segments of coherent motion over the video. More specifically, we have designed a transformer-based network, where we leverage a mathematically well-founded framework, the Evidence Lower Bound (ELBO), to infer the loss function. The loss function combines a flow reconstruction term involving spatio-temporal parametric motion models combining, in a novel way, polynomial (quadratic) motion models for the (x, y) -spatial dimensions and B-splines for the time dimension of the video sequence, and a regularization term enforcing temporal consistency on the masks. We report experiments on four VOS benchmarks with convincing quantitative results. We also highlight through visual results the key contributions on temporal consistency brought by our method.

1 Introduction

When dealing with videos, motion segmentation is one of the key issues. Human beings have the ability to continuously analyze a video and immediately extract the main motion components. Computer vision methods in the deep learning era usually proceed frame by frame. We want to go beyond this classical paradigm and segment the different motion entities in series of flow fields of any length, up to the complete video sequence. We thus thoroughly investigate the temporal dimension of the motion segmentation problem. Since the optical flow (OF) yields all the information on the movement between two images of the video sequence, it is natural to base motion segmentation on optical flow. Motion segmentation is a computer vision task in its own,

but it is also useful for diverse downstream tasks as independent moving object detection, object tracking, or action recognition, to name a few. It is also leveraged in video object segmentation (VOS), while most often coupled with appearance.

The optical flow field at time t enables to get the segmentation at frame t of the video. However, taking a large time window, and even the whole video sequence, is beneficial, since motion entities are generally consistent throughout a video sequence (or at least within every video shot for long videos). Indeed, temporal coherence is inherent to motion. Therefore, it is essential that motion segmentation takes advantage of it, especially in a long-term perspective.

In this paper, we propose an original holistic method for multiple motion segmentation from optical flow over a video sequence. The main contributions of our work are as follows. Our network takes as input a volume of consecutive optical flows, and delivers consistent motion segmentation maps throughout the video sequence. It involves a transformer module allowing for long-term interactions. It is trained in a completely unsupervised manner, without any manual annotation or ground truth data of any kind. The loss function is inferred by leveraging the Evidence Lower Bound (ELBO) framework, and comprises a flow reconstruction term with original spatio-temporal parametric motion models and an additional term enforcing temporal consistency on the segmentation masks. We model with B-splines the long-term temporal evolution of the motion model parameters. Our method also involves a latent representation of the segment motion augmented with positional embedding.

The rest of the paper is organized as follows. Section 2 describes related work regarding motion segmentation. Section 3 presents our unsupervised network for multiple motion segmentation in one go, embedding long-term temporal consistency. In Section 4, we provide implementation details. Section 5 reports results on four VOS benchmarks with a comparison to state-of-the-art unsupervised motion segmentation methods. Finally, Section 6 contains concluding remarks.

2 Related work

Motion segmentation aims to break down each frame of a video sequence into components (or segments) of coherent motion. Usually, each motion segment is identified by a motion model, which can be hand-crafted such as affine or quadratic polynomial models or sometimes learned. Motion segmentation has been investigated for decades [19, 23, 31, 40]. However, we will focus on recent methods in this section. Since accurate and efficient methods for estimating optical flow are now available, motion segmentation methods can leverage optical flow as a reliable input. The advent of deep learning methods in computer vision, and more recently the use of transformer-based networks with attention mechanisms [11], has also encompassed motion segmentation.

In [36], a transformer module, more specifically, the slot attention mechanism introduced in [18], is leveraged to perform motion segmentation from the optical flow. As a matter of fact, it addresses a binary segmentation problem, foreground moving object *vs* background. The loss function is composed of two terms, a flow reconstruction term and an entropy term to make masks as binary as possible. Another approach is adopted in [35] that is able to cope with multiple motion segmentation. Nonlinear subspace

filters are learned from stacked deep multi-layer perceptrons. Then, motion segmentation is inferred at inference by applying K -means to the output embeddings. In [21], the Expectation-Maximization (EM) framework is leveraged to define the loss function and the training procedure for an unsupervised frame-by-frame motion segmentation, where 12-parameter quadratic motion models are involved. The same authors also proposed an extension of that method in [4] to better handle the temporal dimension of the problem, by considering triplets of flows as input. In [37], the authors developed an adversarial method whose aim is to generate a mask hiding the input optical flow, where an inpainter network attempts to recover the flow within the mask. The rationale is that no correct reconstruction of the inside flow can be achieved from the outside flow, if the hidden area exhibits an independent motion and then constitutes a motion segment.

The temporal dimension of motion segmentation has been considered in various ways [31]. Regarding deep learning approaches, motion segmentation at time t is improved at training time in [36], by taking, as input, flows between t and several time instants before and after t . The authors of [8] consider several consecutive RGB frames as input of their self-supervised method. Optical flow is only computed at training time, and the loss function also comprises a temporal consistency term. However, the latter is not applied to two consecutive segmentation masks, but for pairings between the same frame t and another (more or less distant) one. In [9], spatio-temporal transformers were designed for video object segmentation involving temporal feature propagation.

VOS usually requires motion segmentation, often coupled with appearance [5, 10, 38]. It was addressed with supervised or semi-supervised methods as in [7, 9, 12], but also with unsupervised methods [37, 36, 21]. VOS is concerned with the segmentation of primary objects, i.e., object moving in the foreground of a scene and possibly tracked by the camera [41]. Thus, VOS generally involves binary ground truth segregating primary moving object against background. This is for instance the case for the DAVIS2016 benchmark [26]. Recent works have revisited the way of coupling appearance and motion for VOS. The AMD method [17] includes two pathways, the appearance one and the motion one. If it does not use optical flow as input and brings out the objectness concept, it nevertheless relies on a coarse motion representation. In [39], the authors introduce deformable sprites with a video auto-encoder model (optimized at test time), to segment scene elements through the video, by leveraging texture and non-rigid deformations. The work [27] leverages pretrained appearance features (using DINO) and optical flow. The objective function is derived from a form of spectral clustering and applied to the entire video. However, optimization is required at test time. The RCF method [16] involves learnable motion models, and is structured in two stages, a motion-supervised object discovery stage, and a refinement stage with residual motion prediction and high-level appearance supervision. However, the method cannot distinguish objects undergoing different motions. In [6], the prediction of motion patterns is used at training time to learn objectness from videos. The DivA method [2] promotes divided attention. It is based on the same principle as in [37] that motion segments are mutually uninformative, but it is not limited to binary segmentation. It can segment a variable number of moving objects from optical flow, by leveraging a slot attention mechanism guided by the image content through a cross-modal conditional slot decoder.

Our fully unsupervised approach differs from these previous works in several respects. We rely only on optical flow and take a volume of OF fields as input, providing a volume of consistent segmentation maps. We introduce B-splines to define parametric motion models able to correctly handle motion evolution over time, and we express long-term temporal consistency. We infer the loss function from the Evidence Lower Bound (ELBO) framework. In [4], the authors also deal with temporal consistency. However, they only took a triplet of optical flow fields as input, they did not resort to transformers, and the temporal part of the motion model was just a linear (first-order polynomial) model in time. In addition, their temporal linkage of the consecutive motion segmentations over a video sequence was an *ad hoc* post-processing. In contrast, we define a fully integrated long-term model that is end-to-end trained in a unsupervised way. We will call our method LT-MS method, for long-term motion segmentation, and in contrast, we will refer to the method [4] as the ST-MS method, for short-term motion segmentation.

3 Long-term Motion Segmentation Method

We have designed a transformer-based network for multiple motion segmentation from optical flow. It is inspired from the MaskFormer architecture [4], but it only comprises one head corresponding to the mask prediction, as described in Fig.1. The network takes as input a volume, of flexible temporal length, comprising several consecutive optical flow fields. Temporal consistency is expressed in two main ways at the training stage. Firstly, we associate a space-time motion model with each segment to characterize its motion along with the evolution of the latter over time. Secondly, the loss function comprises an additional term enforcing consistent labeling of the motion segments over the volume. Adding the transformer to the latent space of the Unet allows for interaction between distant features in the input, and thus for long-term segmentation. We only incorporate a transformer decoder on the downsampled latent space of the 3D U-net, which induces a limited additional computational load.

3.1 Spatio-temporal parametric motion model

The set of T consecutive flows will be designated as a space-time volume (or volume, to make it short). The volume could even be the whole video sequence. Our space-time motion model is estimated through B-spline functions [33] for its temporal dimension. More precisely, we consider a B-spline function of order n in the variable t over the space-time volume. For the spatial extension, we assign a parametric motion model \tilde{f}_{θ_k} to each motion segment $k, k = 1, \dots, K$, where θ_k specifies the spatial motion model \tilde{f} for segment k . We take $n = 3$. The number L of control points is given by $L = 2 + \lfloor \frac{T-2}{\nu} \rfloor$, where ν manages the temporal frequency of control points. We put a control point at both ends of the volume ($t = 1, t = T$), and the other control points are equidistantly placed between the two. The control points are often not located at time points of the video.

The space-time spline-based motion model is illustrated in Fig.2. Just for this illustration, the motion models are computed within the two segments, foreground moving

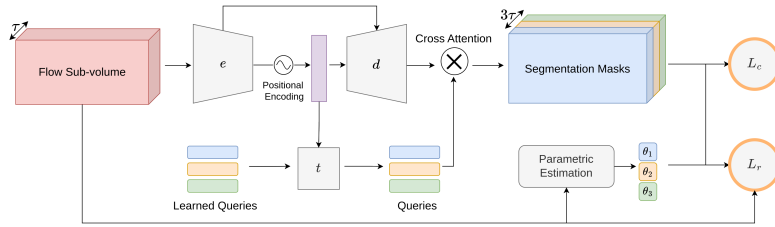


Figure 1: Overall architecture of our multiple motion segmentation method ensuring temporal consistency with the loss term \mathcal{L}_c and the B-spline space-time motion models θ_k (for $k = 1, \dots, K$). It takes as input a volume of T flow fields. It comprises a 3D U-net (e and d boxes) and a transformer decoder (t box). It also involves positional encoding. A cross-attention product yields the K segmentation masks corresponding to the input volume. For the sake of clarity, the block diagram is represented for three motion segments ($K = 3$). \mathcal{L}_r is the flow-reconstruction loss term.

object and background, provided by the ground truth. The estimated motion model for the foreground moving object is able to capture the periodic nature of the swing motion as demonstrated by the plots of the computed motion model parameters. Also, the motion model computed in the background segment perfectly fits the camera motion. Articulated motion (woman’s legs) would require multiple-motion segmentation.

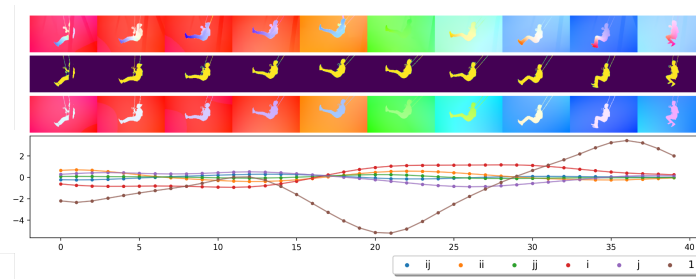


Figure 2: Illustration of the spatiotemporal spline-based motion model. Top row: input flows displayed with the HSV code for the *swing* video of DAVIS2016, binary segmentation ground truth, flows generated by the estimated spline-based motion models for the two segments. Bottom row: plot of the temporal evolution of the six estimated motion model parameters corresponding to the horizontal flow component for the foreground moving object. The x -axis is the video frame index.

Any parametric motion model could be considered. We take a polynomial expansion in the coordinates x and y of any point in the image, with one polynomial for each component of the 2D flow. The use of polynomial is a usual choice for 2D motion modelling, since it is easy to estimate and enables a straightforward physical interpretation. More specifically, we select the 12-parameter quadratic motion model to be able to account for continuously varying depth surface of the objects in the scene,

especially for the whole background, and for complex object or camera motions. In contrast, the affine and the 8-parameter quadratic motion models assume a planar object surface. Indeed, the latter exactly corresponds to the projection in the image of the 3D rigid motion of a planar surface. It is equivalent for velocity fields to the homography transform for points. However, in presence of severe depth effects (strong depth discontinuities) and camera motion, the static scene cannot be represented by a single motion model due to motion parallax produced by static objects located in the foreground. Regarding first the spatial dimension of the motion model, the 2D flow vector yielded by the full quadratic motion model at point (x, y) writes:

$$\tilde{f}_\theta(x, y) = (\theta_1 + \theta_2 x + \theta_3 y + \theta_7 x^2 + \theta_8 xy + \theta_9 y^2, \theta_4 + \theta_5 x + \theta_6 y + \theta_{10} x^2 + \theta_{11} xy + \theta_{12} y^2)^T. \quad (1)$$

B-Splines are modelling the evolution of the parameters of the motion model over time. The resulting motion model at a given time is then a weighted average of the close control ones (each control one being a quadratic model as in eq.(1). By denoting $S_n(\theta_k)$ the subscript of \tilde{f} , we emphasize that the motion model parameters for each segment k are estimated through the B-spline functions:

$$\tilde{f}_{S_n(\theta_k)}(x, y, t) = \sum_{l=1}^L \tilde{f}_{\theta_{k,l}}(x, y) B_{n,l}(t), \quad (2)$$

where $B_{n,l}$ is the l^{th} B-spline, $\theta_{k,l}$ corresponds to the l^{th} control point of the spline, and $\tilde{f}_{\theta_{k,l}}$ is defined by eq.(1).

3.2 Loss function

We consider a volume of optical flow fields $f \in \mathbb{R}^{2 \times T \times W \times H}$, the spatial grid $\Omega \in \mathbb{R}^{W \times H}$ and T temporal steps. We denote $f(i, t) \in \mathbb{R}^2$ the flow associated to site (or point) $i \in \Omega$ ($i = (x, y)$) at time t . We assume that we can decompose the flow as a set of K segments, each one exhibiting a coherent motion. Flow vectors within a given segment k are represented by a smooth parametric motion model parametrized by ϑ_k . Variable $z_{i,t}$ conveys the motion segmentation, $z_{i,t}^k = 1$ if site (i, t) belongs to segment k . z and $\vartheta = \{\vartheta_k, k = 1 \dots K\}$ are latent variables, and f is the observed data. Following [1], we introduce an approximate distribution over segmentation and motion model parameters:

$$q(z, \vartheta | f) = q(z | f) q(\vartheta) = \left(\prod_{t=1}^T \prod_{i \in \Omega} \prod_{k=1}^K q(z_{i,t}^k | f) \right) \left(\prod_k q(\vartheta_k) \right), \quad (3)$$

where $q(\vartheta_k) \triangleq \delta(\theta_k)$ with δ the Dirac distribution and $q(z_{i,t}^k | f) = g_\phi(f)_{i,t}^k$. g_ϕ is our network model taking as input the optical flow volume and returning a probabilistic segmentation volume. We can also write the data-likelihood over a dataset \mathcal{D} of optical

flow volumes f as:

$$\begin{aligned} \log(\mathcal{D}) &= \sum_{f \in \mathcal{D}} \log p(f) = \sum_{f \in \mathcal{D}} (\mathbb{E}_{q(z, \vartheta|f)} [\log \frac{p(f, z, \vartheta)}{q(z, \vartheta|f)}] + KL(q(z, \vartheta|f) || p(z, \vartheta|f))) \\ &\geq \sum_{f \in \mathcal{D}} (\mathbb{E}_{q(z, \vartheta|f)} [\log p(f|z, \vartheta)] - KL(q(z, \vartheta|f) || p(z, \vartheta))), \end{aligned} \quad (4)$$

where we get the Evidence Lower Bound (ELBO). Considering that the flow field can be represented by segment-wise parametric motion models, and assuming conditional independence, we have:

$$p(f|z, \vartheta) = \prod_{t=1}^T \prod_{k=1}^K p(f(t)|\vartheta_k, z) \propto \prod_{t=1}^T \prod_{k=1}^K \prod_{i \in \Omega} \exp(-\|f(i, t) - \tilde{f}_{S_n(\vartheta_k)}(i, t)\|_1 / \xi_{f,t})^{z_{i,t}^k}, \quad (5)$$

where $\tilde{f}_{S_n(\vartheta_k)}(i, t)$ is the flow vector given by the parametric motion model of parameters ϑ_k at point (i, t) as defined in Section 3.1 through the spline approximation and $\xi_{f,t} = \sum_i \|f(i, t)\|_1$ is a normalizing factor. From this likelihood, we can write the left term of the ELBO as:

$$\begin{aligned} \mathcal{L}_r &= -\mathbb{E}_{q(z, \vartheta|f)} [\log p(f|z, \vartheta)] = -\sum_{t=1}^T \sum_k \mathbb{E}_q [\log p(f(t)|\vartheta_k, z)] \\ &= \sum_{t=1}^T \sum_{i \in \Omega} \sum_k g_\phi(f)_{i,t}^k \|f(i, t) - \tilde{f}_{S_n(\vartheta_k)}(i, t)\|_1 / \xi_{f,t} \end{aligned} \quad (6)$$

The term $KL(q(z, \vartheta|f) || p(z, \vartheta))$ allows us to define a prior over the segmentation. We want to enforce the property that the segmentation labels are temporally consistent, i.e., similar between neighbouring frames. We approximate this term using the temporal consistency loss defined in [4], as it showed good experimental results and was efficient to compute at training time. In addition, we provide a mathematical development that motivates this expression in the Appendix. We have:

$$\mathcal{L}_c = \frac{1}{2K|\mathcal{I}|} \sum_{i \in \Omega} \sum_{t=2}^T \mathbb{1}[\|f_{i,t} - f_{i,t-1}\|_1 < \lambda] \sum_{k=1}^K |g_\phi(f)_{i,t}^k - g_\phi(f)_{i,t-1}^k|, \quad (7)$$

The threshold λ allows us to discard occlusion areas. The loss function is thus defined by:

$$\sum_{f \in \mathcal{D}} \mathcal{L}(f, \phi, \theta) = \sum_{f \in \mathcal{D}} \mathcal{L}_r(f, \phi, \theta) + \beta \mathcal{L}_c(f, \phi). \quad (8)$$

We set $\beta = 1$. The training procedure alternatively updates θ and ϕ with α as learning rate:

$$\text{for } f \in \mathcal{D} : \theta^* = \arg \min_{\theta} L(f, \phi, \theta)(f) ; \phi_{t+1} = \phi_t - \alpha \nabla_{\phi} L(f, \phi, \theta^*) \quad (9)$$

3.3 Network architecture

The overall architecture of our unsupervised multiple motion segmentation framework is illustrated in Fig.1. It includes two main modules. The first one, taking the flow volume as input, is a 3D U-net [30]. The latent code augmented with embedding positions is directed to the transformer decoder. Then, by cross-attention, the output formed by the volume of segmentation masks is produced. The training of the overall architecture is based on the minimization of the loss function defined below, while the motion model parameters of the segments are given by the B-spline estimation. Temporal consistency is provided by the loss function and the space-time motion models.

4 Implementation

4.1 Implementation details

Following [6, 16, 21, 4, 36], we adopt the RAFT method [32] to compute the optical flow fields. More specifically, we use the RAFT version trained on the MPI Sintel dataset [2]. We downsample the computed flow fields to feed the network with 128×224 vector fields. The output segmentation maps are upsampled to the initial frame size for evaluation. Thus, we can perform efficient training and inference stages. We typically take flow volumes of temporal length $T = 9$ at training time. However, at test time, we can process flow volumes of larger temporal length, and even the flow volume of the whole sequence. To compute of the spatio-temporal parametric motion models, x and y coordinates are normalized within $[-1, 1]$, and a similar normalization is applied to the t coordinate. The full 12-parameter quadratic motion model is chosen in all the experiments, and we take $\nu = 3$ for the frequency factor in the B-spline approximation. We select for each point (x, y) the segment \hat{k} with the highest prediction. In eq.(7), we set λ as the 99th quantile of the flow differences over the flow volume.

Our LT-MS method is very efficient at test time. The computational time amounts on average to 210 *fps* on a GPU P100, that is, twice as fast as the ST-MS method [4]. It is certainly due to the long flow sequence given as input to the network, which allows for parallelisation of some heavy computations. In addition, our LT-MS architecture remains lightweight, since it combines only three U-net layers and a transformer decoder on the downsampled feature space. Let us also stress that our LT-MS method does not involve any post-processing at all.

4.2 Data augmentation and network training

We applied two types of data augmentation dedicated to optical flow. First, we add a global flow to the input flow similarly as in the EM [21] and ST-MS [4] methods. However, in our case, the global flow is given by a full spline-based spatio-temporal motion model whose parameters are chosen at random. The same global flow is added to the flow fields of a given input volume. It allows us to mimic diverse camera motions, enforcing that the motion segments are independent of it. In addition, we corrupt a few flows out of the nine input ones. Thus, we simulate poorly estimated flow fields at some time instants, and the temporal consistency should overcome it.

Our motion segmentation method is fully unsupervised. We never use any manual segmentation annotation. We train our model using the FlyingThings3D (FT3D) dataset [20]. Our (demanding) objective is to demonstrate the high generalization power of our model. We train our model once for all on the optical flow fields computed on FT3D, and then, apply it on new unseen datasets. For hyperparameter setting, we select the stopping epoch from the loss function evaluated on the DAVIS2016 training set. Additional information on the optimization stage in eq.(9) is given in the Appendix. We trained on a single Quadro RTX 6000 for 77h with a batch size of 5 on 32k flow fields computed on FT3D.

5 Experimental Results

We have carried out experiments on four datasets: DAVIS2016¹ [26], SegTrackV2² [15], FBMS59 [24], and DAVIS2017-motion [5]. Information on the datasets is provided in the Appendix.

5.1 Ablation study

We have conducted an ablation study to assess three main components of our method LT-MS with four masks ($K = 4$), in particular related to the temporal dimension of the problem. We have changed one component at a time as specified hereafter. We use the polynomial space-time quadratic motion model of ST-MS [4] instead of the space-time motion model based on B-splines over the input sequence. We omit the consistency term \mathcal{L}_c in the loss function. We just take the convnet without the transformer decoder. All the ablation experiments were run on the three datasets, DAVIS2016, FBMS59, SegTrackV2. Results are collected in Table 1. In addition, we performed them for two input sequence configurations, respectively input sequences of ten flows, and input sequence of 120 flows (in practice, the whole video for the DAVIS2016 dataset). We can observe that the three ablations have almost the same impact on the performance. The three corresponding model components, i.e., the spline-based motion model, the temporal-consistency loss term, and the transformer decoder are thus all beneficial in similar proportions. They are able to handle the temporal dimension of the problem and the temporal motion evolution along the sequence in a compelling way. Admittedly, the contributions of these three components are more significant for the FBMS59 and the SegTrackV2 datasets. However, the dynamic content of the majority of the DAVIS2016 videos, and then, the overall performance score cannot allow to fully appreciate the contributions of the three model components. Yet, they can be acknowledged by visualizing results obtained on some videos of DAVIS2016, as shown in the Appendix.

5.2 Quantitative and comparative evaluation

We report in Table 2 the results obtained by two versions of our LT-MS method on the three datasets DAVIS2016, SegTrackV2, and FBMS59. LT-MS-K2 performs segmen-

¹<https://davischallenge.org/index.html>

²<https://paperswithcode.com/dataset/segtrack-v2-1>

Table 1: Ablation study for three main components of our method LT-MS ($K = 4$) on DAVIS2016, FBMS59 and SegTrackV2. Only one model component is modified at a time. The performance scores are given by the Jaccard index \mathcal{J} . We report ablation results with two input-flow sequence length (or cut size), respectively, by dividing the video into pieces of ten successive frames or by considering 120 successive frames (in practice, the whole video for DAVIS2016).

Ablation / Dataset	DAVIS2016		FBMS59		SegTrackv2	
	10	120	10	120	10	120
Full Model LT-MS-K4	74.8	72.4	61.0	58.2	61.3	60.4
Unet3D only	73.0	71.3	56.6	55.5	58.2	57.3
No consistency term \mathcal{L}_c	73.5	71.0	57.5	55.5	58.0	57.5
Polynomial space-time quadratic model	73.4	69.8	57.4	54.5	57.8	56.6

tation with only two masks ($K = 2$) while LT-MS-K4 involves four masks ($K = 4$). Table 2 collects results obtained by our LT-MS method and other existing unsupervised methods, when available. We follow the categorization proposed in [21] regarding input and training. However, we have added a category w.r.t. the network input for four recent methods, [6, 8, 16, 17], that only use RGB images as input at test time, the optical flow being only involved in the loss function. Evaluation is performed on the binary ground truth (foreground moving object *vs* background) for the three datasets. In the Appendix, we explain how we select the segments for the binary evaluation from the multiple motion segments delivered by our LT-MS method. We still put the OCLR method [5] in the category of unsupervised methods, whereas the authors of the DivA method [2] did not. Indeed, OCLR is not fully unsupervised, since it relies on human-annotated sprites to include realistic shapes in the computer-generated data used at training time. We consider the OCLR version taking only optical flow as input. The post-processing added to the CIS method [37], based on Conditional Random Fields (CRF), is an heavy one, which leads most authors to retain only the version without post-processing for a fair comparison.

As shown in Table 2, our LT-MS method provides very convincing results, both for LT-MS-K2 and LT-MS-K4, in the category of unsupervised methods based on optical flow only. Besides, we report a repeatability study in the Appendix. OCLR and DivA demonstrate better performance on the SegTrackV2 dataset. However, as aforementioned, OCLR is not a fully unsupervised method, while DivA leverages RGB images in its conditional decoder. In addition, DivA, along with MoSeg and CIS methods, takes multi-step flows as input between t and in turn $t + 1$, $t + 2$, $t - 1$, $t - 2$, and averages the four corresponding predictions to get the final result. SegTrackV2 includes sequences acquired with a poorly controlled handheld camera, which leads to unstable sequences where the contribution of our method is therefore less likely to be emphasized. Failure cases may occur for very complex motion (ripples on the water), or with a particularly strong temporal evolution (an object approaching the camera from afar quickly and closely).

Overall, temporal consistency is properly handled over long temporal periods by our LT-MS method. Beyond segmentation performance, we want to stress that our

Table 2: Results obtained with two versions of our LT-MS method on DAVIS2016, SegTrackV2, FBMS59. LT-MS-K2 performs segmentation with two masks ($K = 2$), and LT-MS-K4 involves four masks ($K = 4$). We include comparison with unsupervised methods (scores from cited articles). All scores corresponds to evaluation on the binary ground-truth. For LT-MS-K4 and LT-MS-K2, we report results obtained with a cut size of 10. Results with a cut size of 120 are given for LT-MS-K4 in Table 1 with very close performance (additional results on this point in the Appendix). The Jaccard index \mathcal{J} is the intersection over union between the extracted segments and the ground truth, while \mathcal{F} focuses on segment boundary accuracy. Performance is assessed by the average score over all samples, for all datasets but DAVIS2016. For the latter, the overall score is given by the average of sequence scores. *Actually, putting OCLR as an unsupervised method can be questionable (see main text). †DivA somehow uses RGB input since its conditional decoder leverages input images.

Method	Training	Input	DAVIS2016		SegTrack V2	FBMS59	
			$\mathcal{J} \uparrow$	$\mathcal{F} \uparrow$	$\mathcal{J} \uparrow$	$\mathcal{J} \uparrow$	
Ours LT-MS-K4	Unsupervised	Flow	74.8	72.2	61.3	61.0	
Ours LT-MS-K2			70.3	68.5	58.6	55.3	
ST-MS (4 masks) [4]			73.2	70.3	55.0	59.4	
EM [21]			69.3	70.7	55.5	57.8	
MoSeg [36]			68.3	66.1	58.6	53.1	
FTS [25]			55.8	-	47.8	47.7	
TIS ₀ [10]			56.2	45.6	-	-	
OCLR* [5] (flow only)			72.1	-	67.6	65.4	
GWM [6]			RGB (Flow in loss)	79.5	-	78.3	77.4
RCF [16]				80.9	-	76.7	69.9
AMD [17]		57.8		-	57.0	47.5	
MOD [8]		73.9		-	62.2	61.3	
DivA(4)† [2]		RGB & Flow	72.4	-	64.6	-	
TIS _s [10]			62.6	59.6	-	-	
CIS - No Post [37]			59.2	-	45.6	36.8	
CIS - With Post [37]			71.5	-	62.0	63.6	

method is the only one providing *by design* a coherent segmentation over the sequence, which is a significant added value for downstream tasks, like tracking or dynamic scene interpretation.

5.3 Multi-segment evaluation

We have also performed the evaluation of multiple motion segmentation for a multi-segment setting. Since multiple-motion segmentation is harder than the binary motion segmentation (moving foreground *vs* background), accuracy scores are expected to decrease for all methods. In Table 3, we report comparative results on the DAVIS2017-motion dataset and on FBMS59. As for the other methods, we performed segmentation with three masks. To this end, we finetuned the LT-MS-K4 network on the DAVIS2016 training set with now three masks ($K = 3$). The resulting performance on DAVIS2017-motion is slightly better than ST-MS [4], and far better than MoSeg. There is still the same remark about OCLR status as an unsupervised method. Regarding FBMS59, we report multimask segmentation results with two different metrics. Our LT-MS method

Table 3: Multi-segment evaluation. Evaluation is performed on the video as a whole following the official DAVIS2017 scheme. Reported scores are the average of the individual video scores. $\mathcal{J}\&\mathcal{F}$ is the mean of the two. For FBMS59, the evaluation metrics are bootstrap IoU (bIoU) [2] where each ground-truth mask is mapped to the most likely predicted segment (performed at the frame level), and linear assignment that is a bilinear mapping between the ground-truth and the predicted segments at the sequence level (as in the official DAVIS2017 evaluation). *See caption of Table 2.

Dataset	DAVIS2017-motion			FBMS59	
	$\mathcal{J}\&\mathcal{F} \uparrow$	$\mathcal{J} \uparrow$	$\mathcal{F} \uparrow$	bIoU	Linear Assignment
Ours LT-MS-K3	42.2	39.3	45.0	58.4	47.2
ST-MS [4]	42.0	38.8	45.2	-	-
MoSeg [36]	35.8	38.4	33.2	-	-
OCLR* [5]	55.1	54.5	55.7	-	-
DivA [2]	-	-	-	42.0	-

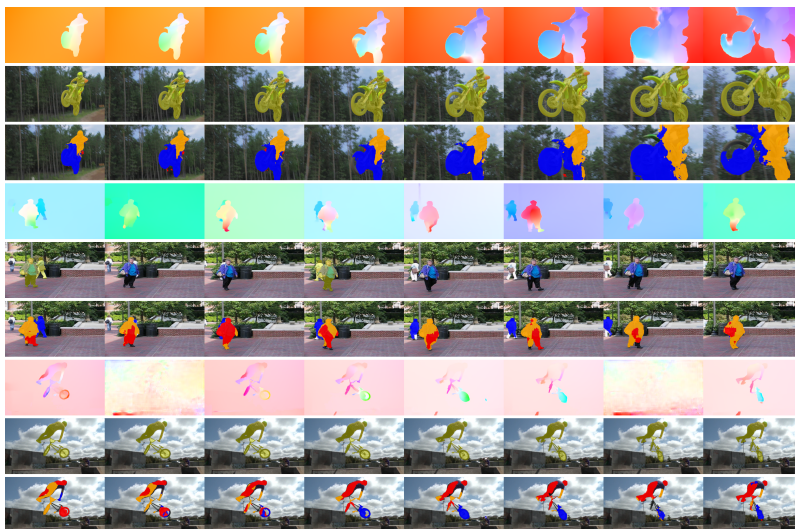


Figure 3: Results obtained with our LT-MS-K4 method for *motocross-jump* from DAVIS2016, *people02* from FBMS59 and *bmx* from SegTrackV2. For each group, the first row samples flow fields (HSV color code) corresponding to the processed video. The second row contains the corresponding images of the video, where ground-truth of the moving object is overlaid in yellow. The third row shows the motion segments provided by our LT-MS-K4 method with one colour per segment. We constantly adopt the same color set for the three masks corresponding to moving objects (blue, red and orange), and we let the image for the background mask.

outperforms by a large margin DivA [2] that attempted this multi-segment evaluation on FBMS59.

5.4 Qualitative visual evaluation

Fig.3 contains several visual results to demonstrate how our LT-MS method behaves on different situations. We display three result samples obtained on different videos of the benchmarks. Additional results are provided in the Appendix. We can observe that the motion segments are globally accurate. Since our method involves several masks, we can properly handle articulated motions (*people2*, *bmx*), deal with the presence of several moving objects in the scene (*people2*), separate the rider from the bike or motorbike (*bmx*, *motocross-jump*), or accomodate motion parallax. Since our method enforces temporal consistency, it can also deal with errors in optical flow estimation or with objects that momentarily stop moving (*bmx*). We must keep in mind that our actual target is the optical-flow segmentation (OFS) task, even if we evaluate our method on VOS benchmarks. When VOS benchmarks deal with the segmentation of one primary object moving in the foreground, it may occur discrepancies with OFS, which negatively impacts the evaluation scores. The segmentation of additional moving parts, wrong for VOS ground truth, makes sense from the OFS standpoint.

6 Conclusion

We have designed an original transformer-based unsupervised method for segmenting multiple motions over a video, without any postprocessing. It performs it in one go, which is a more demanding goal, but provides decisive added value regarding for instance tracking or dynamic scene interpretation. Our LT-MS method leverages the ELBO framework for the loss function, and fully acknowledges the temporal dimension of the motion segmentation problem. Our method delivers a stable and consistent OF segmentation throughout long video sequences. It introduces at training time B-splines spatio-temporal parametric motion models over space-time volumes, and a loss term expressing temporal consistency over successive masks while taking care of occlusions. Our transformer-based network can be applied at test time to input volumes of any time length. It can accomodate different choices on the number K of masks with a simple fine-tuning step. Experimental results on several datasets demonstrate the efficiency and the accuracy of our LT-MS method by providing competitive results on several datasets. In addition, it is very fast at test time.

References

- [1] G.K. Batchelor. *An introduction to fluid dynamics*. Cambridge University Press, 1967.
- [2] D.J. Butler, J. Wulff, G.B. Stanley, and M.J. Black. A naturalistic open source movie for optical flow evaluation, In *European Conference on Computer Vision (ECCV)*, 2012.
- [3] M. Caron, H. Touvron, I. Misra, H. Jégou, J. Mairal, P. Bojanowski, and A. Joulin. Emerging properties in self-supervised vision transformers. In *International Conference on Computer Vision (ICCV)*, October 2021.
- [4] B. Cheng, A. G. Schwing, and A. Kirillov. Per-pixel classification is not all you need for semantic segmentation. In *Conference on Neural Information Processing Systems (NeurIPS)*, 2021.
- [5] J. Cheng, Y.-H. Tsai, S. Wang, and M.-H. Yang. Segflow: Joint learning for video object segmentation and optical flow. In *International Conference on Computer Vision (ICCV)*, Venice, 2017.
- [6] S. Choudhury, L. Karazija, I. Laina, A. Vedaldi, and C. Rupprecht. Guess what moves: Unsupervised video and image segmentation by anticipating motion. *British Machine Vision Conference (BMVC)*, London, 2022.
- [7] A. Dave, P. Tokmakov, and D. Ramanan. Towards segmenting anything that moves. In *Int. Conference on Computer Vision Workshops (ICCVW)*, Seoul, 2019.
- [8] S. Ding, W. Xie, Y. Chen, R. Qian, X. Zhang, H. Xiong, and Q. Tian. Motion-inductive self-supervised object discovery in videos. *arxiv.org/abs/2210.00221*, October 2022.
- [9] B. Duke, A. Ahmed, C. Wolf, P. Aarabi, and G. W. Taylor. SSTVOS: Sparse spatiotemporal transformers for video object segmentation. In *Conference on Computer Vision and Pattern Recognition (CVPR)*, 2021.
- [10] B. Griffin and J. Corso. Tukey-inspired video object segmentation. In *IEEE Winter Conference on Applications of Computer Vision (WACV)*, Waikoloa Village, January 2019.
- [11] K. Han, Y. Wang, H. Chen, X. Chen, J. Guo, Z. Liu, Y. Tang, A. Xiao, C. Xu, Y. Xu, Z. Yang, Y. Zhang, and D. Tao. A survey on vision transformer. *IEEE Transactions on Pattern Analysis and Machine Intelligence*, 45(1):87-110, January 2023.
- [12] S.D. Jain, B. Xiong, and K. Grauman. FusionSeg: Learning to combine motion and appearance for fully automatic segmentation of generic objects in videos. In *Conference on Computer Vision and Pattern Recognition (CVPR)*, Honolulu, 2017.
- [13] D.P. Kingma and M. Welling. An introduction to variational autoencoders. *Foundations and Trends in Machine Learning*, 12(4):307-392, 2019.
- [14] D. Lao, Z. Hu, F. Locatello, Y. Yang, and S. Soatto. Divided attention: Unsupervised multi-object discovery with contextually separated slots. *arXiv:2304.01430*, April 2023.
- [15] F. Li, T. Kim, A. Humayun, D. Tsai, and J. M. Rehg. Video segmentation by tracking many figure-ground segments. In *International Conference on Computer Vision (ICCV)*, Sydney, 2013.
- [16] L. Lian, Z. Wu, S. X. Yu. Bootstrapping objectness from videos by relaxed common fate and visual grouping. *Conference on Computer Vision and Pattern Recognition*, Vancouver, June 2023.
- [17] R. Liu, Z. Wu, S. X. Yu, and S. Lin. The Emergence of objectness: Learning zero-shot segmentation from videos. In *Conference on Neural Information Processing Systems (NeurIPS)*, 2021.

- [18] F. Locatello, D. Weissenborn, T. Unterthiner, A. Mahendran, G. Heigold, J. Uszkoreit, A. Dosovitskiy, and T. Kipf. Object-centric learning with slot attention. In *Conference on Neural Information Processing Systems (NeurIPS)*, 2020.
- [19] J. Mattheus, H. Grobler, and A. M. Abu-Mahfouz. A review of motion segmentation: Approaches and major challenges. *International Multidisciplinary Information Technology and Engineering Conference (IMITEC)*, November 2020.
- [20] N. Mayer, E. Ilg, P. Häusser, P. Fischer, D. Cremers, A. Dosovitskiy and T. Brox. A large dataset to train convolutional networks for disparity, optical flow, and scene flow estimation. In *Conference on Computer Vision and Pattern Recognition (CVPR)*, Las Vegas, June 2016.
- [21] E. Meunier, A. Badoual and P. Bouthemy. EM-driven unsupervised learning for efficient motion segmentation. In *IEEE Transactions on Pattern Analysis and Machine Intelligence*, 45(4):4462-4473, April 2023.
- [22] E. Meunier and P. Bouthemy. Unsupervised space-time network for temporally-consistent segmentation of multiple motions. In *Conference on Computer Vision and Pattern Recognition (CVPR)*, Vancouver, June 2023.
- [23] A. Mitiche and P. Bouthemy. Computation and analysis of image motion: A synopsis of current problems and methods. *International Journal of Computer Vision*, 19(1):29-55, 1996.
- [24] P. Ochs, J. Malik, and T. Brox. Segmentation of moving objects by long term video analysis. *IEEE Transactions on Pattern Analysis and Machine Intelligence*, 36(6):1187-1200, June 2014.
- [25] A. Papazoglou and V. Ferrari. Fast object segmentation in unconstrained video. In *IEEE International Conference on Computer Vision (ICCV)*, Sydney, December 2013.
- [26] F. Perazzi, J. Pont-Tuset, B. Mc Williams, L. Van Gool, M. Gross, and A. Sorkine-Hornung. A benchmark dataset and evaluation methodology for video object segmentation. In *Conf. on Computer Vision and Pattern Recognition (CVPR)*, Las Vegas, June 2016.
- [27] G. Ponimatkin, N. Samet, Y. Xiao, Y. Du, R. Marlet, and V. Lepetit. A simple and powerful global optimization for unsupervised video object segmentation. In *Winter Conference on Applications of Computer Vision (WACV)*, Waikoloa, Jan. 2023.
- [28] J. Pont-Tuset, F. Perazzi, S. Caelles, P. Arbeláez, A. Sorkine-Hornung, and L. Van Gool. The 2017 Davis challenge on video object segmentation. *arXiv:1704.00675*, 2017.
- [29] A. Ranjan, V. Jampani, L. Balles, K. Kim, D. Sun, J. Wulff, and M.J. Black. Competitive collaboration: Joint unsupervised learning of depth, camera motion, optical flow and motion segmentation. In *Conf. on Computer Vision and Pattern Recognition (CVPR)*, Long Beach, 2019.
- [30] O. Ronneberger, P. Fischer, and T. Brox. U-net: Convolutional networks for biomedical image segmentation. In *Int. Conf. on Medical Image Computing and Computer Assisted Intervention (MICCAI)*, Munich, October 2015.
- [31] D. Sun, E. B. Sudderth, and M. J. Black. Layered segmentation and optical flow estimation over time. In *Conference on Computer Vision and Pattern Recognition (CVPR)*, Providence, June 2012.
- [32] Z. Teed and J. Deng. RAFT: Recurrent all-pairs field transforms for optical flow. In *European Conference on Computer Vision (ECCV)*, 2020.

- [33] M. Unser. Splines: A perfect fit for signal and image processing. *Signal Processing Magazine*, 16(6):22-38, November 1999.
- [34] J. Xie, W. Xie, and A. Zisserman. Segmenting moving objects via an object-centric layered representation. In *Conference on Neural Information Processing Systems (NeurIPS)*, 2022.
- [35] X. Xu, L. Zhang, L.-F. Cheong, Z. Li, and C. Zhu. Learning clustering for motion segmentation. *IEEE Transactions on Circuits and Systems for Video Technology*, 32(3):908-919, March 2022.
- [36] C. Yang, H. Lamdouar, E. Lu, A. Zisserman, and W. Xie. Self-supervised video object segmentation by motion grouping. In *International Conference on Computer Vision (ICCV)*, October 2021.
- [37] Y. Yang, A. Loquercio, D. Scaramuzza, and S. Soatto. Unsupervised moving object detection via contextual information separation. In *Conference on Computer Vision and Pattern Recognition (CVPR)*, Long Beach, 2019.
- [38] Y. Yang, B. Lai, and S. Soatto, DyStaB: Unsupervised object segmentation via dynamic-static bootstrapping. In *Conference on Computer Vision and Pattern Recognition (CVPR)*, 2021.
- [39] V. Ye, Z. Li, R. Tucker, A. Kanazawa, and N. Snavely. Deformable sprites for unsupervised video decomposition. In *Conference on Computer Vision and Pattern Recognition (CVPR)*, New Orleans, 2022.
- [40] L. Zappella, X. Llado, and J. Salvi Motion segmentation: A review. *Frontiers in Artificial Intelligence and Applications*, 184:(398-407), January 2008.
- [41] T. Zhou, F. Porikli, D.J. Crandall, L. Van Gool, and W. Wang. A survey on deep learning technique for video segmentation. *IEEE Transactions on Pattern Analysis and Machine Intelligence*, 45(6):7099-7122, June 2023.

A Appendix

A.1 Loss function

Here, we motivate the expression of the temporal consistency term \mathcal{L}_c of the loss function, given by Eq.7 in the main text.

First, let us recall the main definitions and notations. We consider a volume of optical flow fields $f \in \mathbb{R}^{2 \times T \times W \times H}$, the spatial grid $\Omega \in \mathbb{R}^{W \times H}$ and T temporal steps. We assume that we can decompose the flow as a set of K segments, each one exhibiting a coherent motion. Flow vectors within a given segment k can be represented by a smooth parametric motion model parametrized by θ_k . $\theta = \{\theta_k, k = 1 \dots K\}$. Variable $z_{i,t}$ conveys the motion segmentation, $z_{i,t}^k = 1$ if site (i, t) belongs to segment k ($z_{i,t}^k = 0$ otherwise). z and θ are latent variables, and f is the observed data.

A.1.1 Prior

We introduce a prior on z :

$$\begin{aligned} \forall i \in I, \forall t \in \{1 \cdots T\}, z_{i,t} &\in \{1 \cdots K\} \\ p(z) &= \prod_i p(z_{i,1}) \prod_{t=2}^T p(z_{i,t}|z_{i,t-1}) \\ p(z_{i,t} = k | z_{i,t-1} = l) &= \frac{1}{M} \exp(\alpha \mathbb{1}[k = l] + \beta \mathbb{1}[k \neq l]) \\ p(z_{i,1} = k) &= \frac{1}{K}. \end{aligned}$$

We also use the notation $g_{i,t}^k = g_\phi(f)_{i,t}^k = q(z_{i,t} = k | f)$.

Using an uninformative prior on θ , we can compute the KL term as:

$$KL[q(z, \theta | f) | p(z, \theta)] = KL[q(z | f) | p(z)] \quad (10)$$

$$= \mathbb{E}_q[\log q(z | f)] - \mathbb{E}_q[\log p(z)] \quad (11)$$

$$\mathbb{E}_q[\log q(z | f)] = \sum_{i,t,k} g_{i,t}^k \log g_{i,t}^k \quad (12)$$

$$\mathbb{E}_q[\log p(z)] = \sum_i [\mathbb{E}_q[\log p(z_{i,1})]] + \sum_{t=2}^T \mathbb{E}_q[\log p(z_{i,t} | z_{i,t-1})] \quad (13)$$

$$= \sum_i \sum_{t=2}^T \mathbb{E}_q[\log p(z_{i,t} | z_{i,t-1})] - I \log(K) \quad (14)$$

$$= \sum_i \sum_{t=2}^T \sum_k \sum_l g_{i,t}^k g_{i,t-1}^l (\alpha \mathbb{1}[k = l] + \beta \mathbb{1}[k \neq l]) + c, \quad (15)$$

where $c = -I(\log(K) + T \log(M))$ is a constant.

We set $\beta = 0$, knowing that $\alpha > 0$:

$$\mathbb{E}_q[\log p(z)] = \alpha \sum_i \sum_{t=2}^T \sum_k g_{i,t}^k g_{i,t-1}^k + c. \quad (16)$$

A.1.2 Approximation

$$2 * g_{i,t}^k g_{i,t-1}^k = -(g_{i,t}^k - g_{i,t-1}^k)^2 + (g_{i,t}^k)^2 + (g_{i,t-1}^k)^2 \quad (17)$$

Thus, we can write:

$$\mathbb{E}_q[\log p(z)] = \frac{\alpha}{2} \sum_i \sum_{t=2}^T \sum_k -(g_{i,t}^k - g_{i,t-1}^k)^2 + (g_{i,t}^k)^2 + (g_{i,t-1}^k)^2 + c. \quad (18)$$

$$\begin{aligned} \mathbb{E}_q[\log p(z)] &= \frac{\alpha}{2} \left(\sum_i \sum_{t=2}^T \sum_k -(g_{i,t}^k - g_{i,t-1}^k)^2 \right. \\ &\quad \left. + \sum_i \sum_{t=1}^T \sum_k (g_{i,t}^k)^2 + \sum_i \sum_{t=2}^{T-1} \sum_k (g_{i,t}^k)^2 \right) \quad (19) \end{aligned}$$

Thus, we get:

$$\begin{aligned}
KL[q(z|f)||p(z)] &= \frac{\alpha}{2} \sum_i \sum_{t=2}^T \sum_k (g_{i,t-1}^k - g_{i,t}^k)^2 + \sum_i \sum_{t=1}^T \sum_k g_{i,t}^k * (\log(g_{i,t}^k)) \\
&\quad - \frac{\alpha}{2} * g_{i,t}^k - \frac{\alpha}{2} \sum_i \sum_{t=2}^{T-1} \sum_k (g_{i,t}^k)^2 + c.
\end{aligned} \tag{20}$$

$\forall x \in [0, 1]; \alpha > 0 : -\frac{\alpha}{2} \leq x(\log x - \frac{\alpha}{2}x) \leq 0$, therefore:

$$KL[q(z|f)||p(z)] \leq \frac{\alpha}{2} \sum_{i,t,k} (g_{i,t}^k - g_{i,t-1}^k)^2 + c$$

A.1.3 Combining with likelihood

$$\begin{aligned}
Elbo(f) &= \mathbb{E}_{q(z,\theta|f)} [\log p(f|z, \theta)] - KL(q(z, \theta|f)||p(z, \theta)) - c \\
Elbo(f) &\geq \mathbb{E}_{q(z,\theta|f)} [\log p(f|z, \theta)] - \frac{\alpha}{2} \sum_i \sum_{t=2}^T \sum_k (g_{i,t}^k - g_{i,t-1}^k)^2 - c
\end{aligned}$$

As $\forall x, y \in [0, 1]^2 : |x - y| \geq (x - y)^2$:

$$Elbo(f) \geq \mathbb{E}_{q(z,\theta|f)} [\log p(f|z, \theta)] - \frac{\alpha}{2} \sum_i \sum_{t=2}^T \sum_k |g_{i,t}^k - g_{i,t-1}^k| - c \tag{21}$$

$$Elbo(f) \geq - \sum_{t=1}^T \sum_{i \in \Omega} \sum_k g_\phi(f)_{i,t}^k \|f(i, t) - \tilde{f}_{S_n(\theta_k)}(i, t)\|_1 / \xi_{f,t} \tag{22}$$

$$- \frac{\alpha}{2} \sum_{i,t=2,k} |g_{i,t}^k - g_{i,t-1}^k| - c \tag{23}$$

This is the lower bound we are maximising, although, in practice we are not accounting a fraction of the sites to deal with occlusion areas.

A.1.4 Experimental validation

In order to evaluate how similar the objective we trained in the paper is to the expression defined in Eq.7 above, we train a model minimizing the following loss function:

$$\begin{aligned}
\mathcal{L} &= \sum_{t=1}^T \sum_{i \in \Omega} \sum_k g_\phi(f)_{i,t}^k \|f(i, t) - \tilde{f}_{S_n(\theta_k)}(i, t)\|_1 / \xi_{f,t} \\
&\quad - \alpha \sum_i \sum_{t=2}^T \sum_k g_{i,t}^k g_{i,t-1}^k + \beta \sum_{t=1}^T \sum_{i \in \Omega} \sum_k g_\phi(f)_{i,t}^k \log g_\phi(f)_{i,t}^k
\end{aligned} \tag{24}$$

In practice, we use $\alpha = 0.5$ and $\beta = 0.01$, and we obtain the results reported in Table 4.

Table 4: Comparison of the two losses

Prior / Dataset	DAVIS2016		FBMS59		SegTrackv2	
	10	120	10	120	10	120
Full Model LT-MS-K4	74.8	72.4	61.0	58.2	61.3	60.4
Prior Eq.7	73.5	71.6	57.6	55.6	59.0	57.4

A.2 Datasets

DAVIS2016 comprises 50 videos (for a total of 3455 frames), depicting diverse moving objects. It is split in a training set of 30 videos and a validation set of 20 videos. Only the primary moving object is annotated in the ground truth. The criteria for evaluation on this dataset are the Jaccard score \mathcal{J} (intersection-over-union), and the contour accuracy score \mathcal{F} , the higher, the better for both. FBMS59 includes 59 videos (720 annotated frames), and SegTrackV2 14 videos (1066 annotated frames). Both mostly involve one foreground moving object, but sometimes a couple of moving objects. For FBMS59, we use the 30 sequences of the validation set. Although annotations may comprise multiple objects, the VOS community exploits FBMS59 and SegTrackV2 similarly as DAVIS2016, considering a binary ground-truth, by grouping moving objects in the foreground. We follow this practice. However, we also provide a multi-mask evaluation for FBMS59.

DAVIS2017 is an extension of DAVIS2016, containing 90 videos. It includes additional videos with multiple moving objects, and it provides multiple-segment annotations for the ground truth. It is split into 60 videos for training and 30 for evaluation. DAVIS2017-motion is a curated version of the DAVIS2017 dataset proposed in [5] for a fair evaluation of methods based on optical flow only. Connected objects exhibiting the same motion are merged in the ground truth for evaluation. We proceed to the evaluation with the official algorithm that involves a Hungarian matching process.

A.3 Addition to the ablation study

Fig.4 plots the performance scores for the three ablations when the length of the input flow sequence varies from 10 to 120. Overall, they exhibit comparable behaviour at a certain distance from the full model.

Visual results reported in Fig.5 clearly demonstrate that the addition of the temporal consistency loss term \mathcal{L}_c allows us to get far more consistent segments over time, whether for the background, or the moving objects. For instance, in the fourth example, the foreground moving car is perfectly segmented throughout the sequence along with its wheels, and (small) moving cars in the background. Fig.9 highlights the contribution of the spline-based motion model on the *dog* video, and its obvious ability to handle motions that do not vary uniformly, as the erratic movement of the dog.

A.4 Optimization implementation

We use Adam optimizer with the following strategy on the learning rate α to train the network (3D Unet and transformer), inspired from the warmup-decay strategy in [5]. We linearly increase it from 0 to $1e - 4$ for 20 epochs, then, we divide it by two every 40 epochs. The estimation of the motion model parameters through the B-spline approximation at training time is achieved with the Pytorch implementation of L-BGFS [3]. Indeed, as written in eq.2 of the paper, the

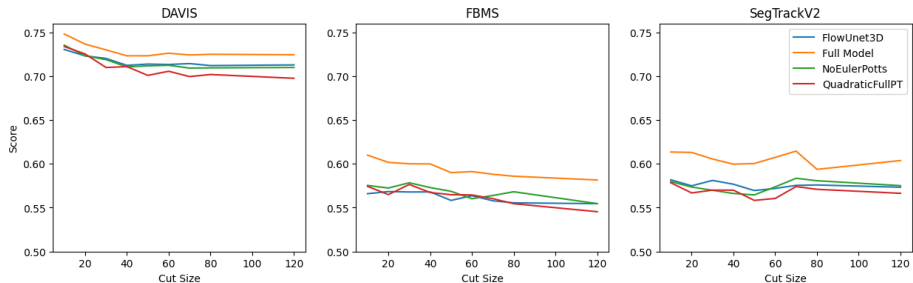


Figure 4: Influence of the length of the input flow sequence (also referred to as cut size on the horizontal axis of the plot) on the three modified versions of our LT-MS-K4 method with comparison with the full model. Left plot: for the DAVIS2016 dataset. Middle plot: for the FBMS59 dataset. Right plot: for the SegTrackV2 dataset. Overall, they exhibit comparable behaviour at a certain distance from the full model.

parametric models induced over time by the splines are a linear combination of quadratic parametric models. Thus, we can optimize eq.6 of the paper to obtain the argmin in eq.9, which is a convex problem.

A.5 Segment selection for evaluation

VOS and OFS are close but not identical tasks. However, we use VOS benchmarks, since no OFS benchmarks are available. Let us recall that the VOS one is attached to the notion of a primary object of interest moving in the foreground (sometimes, a couple of objects). As a consequence, we have to select the right segments to cope with the binary ground truth of the VOS benchmarks, as usually done for the DAVIS2016, SegTrackV2 and FBMS59 datasets.

Since we deal with multiple-motion segmentation, i.e., K segments, we have to group them into two clusters corresponding to the foreground moving object on one side and the background on the other side. We proceed as in the ST-MS method [4]. However, in our case, we can directly evaluate our LT-MS method in one shot over the predicted segmentation sequence, since there is no temporal linking postprocessing for LT-MS. For evaluations with $K = 2$, we do not need to group the masks, so we just set one of the masks as foreground using Hungarian matching over the sequence (alternatively, we could just pick the smallest of the two masks). Regarding the evaluation on the DAVIS2017-motion dataset whose ground truth is not binary, we use the official evaluation script (which perform hungarian matching over the sequence) to associate each predicted segment k with the ground-truth annotations, knowing that we have to consider $K = 3$ masks for this experimentation.

A.6 Multi-mask evaluation in FBMS59

We implement the "Bootstrap IoU" score to evaluate multi-mask segmentation in FBMS59, as described in [2]³ The core idea is to match each ground-truth segment to the most likely segment (i.e., with the one of highest IoU). Let us note that this evaluation includes the background segment, since background is not identified in the FBMS59 multi-mask annotation. The algorithm we used for evaluation is detailed in Fig. 6.

³We use the multi-label ground truth provided by Dong Lao, first author of [2].

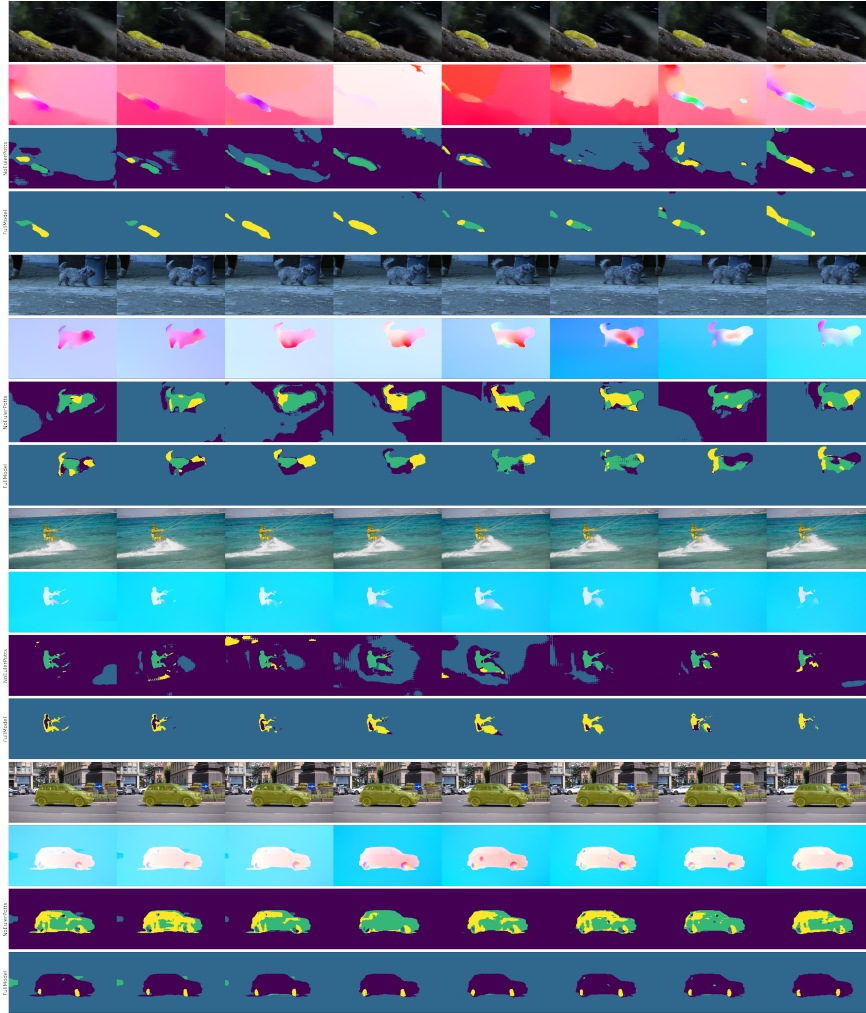


Figure 5: Four groups of qualitative results regarding the ablation of the temporal-consistency loss term. They respectively correspond to the *worm* video of SegTrackV2, the *dogs01* video of FBMS59, and the *kite-surf* and *car-roundabout* videos of DAVIS2016. For each group, the first row contains sample images with the segmentation ground-truth, when available at that frame, overlaid in yellow, the second row displays the input flows, the third and fourth rows show the predicted motion segmentations, respectively without and with the temporal consistency loss term. Clearly, this model component allows us to get far more consistent segments over time.

```

1 sequences_iou = []
2 for sequence in dataset :
3     objects_iou = []
4     for frame in sequence :
5         for x in gt_annotatons_including_background :
6             maxiou = 0
7             for y in predicted_segments :
8                 maxiou = max(maxiou, iou(x, y))
9             objects_iou.append(maxiou)
10            sequence_iou.append(mean(objects_iou))
11 dataset_iou = mean(sequences_iou)

```

Figure 6: Algorithm Evaluation bIoU.

For the linear assignment score, we find the best bipartite sequence-level match between the ground truth and the predictions. Similar to the bIoU evaluation, we compute the score with all the labels of the ground truth. This evaluation is more demanding, because it forces a one-to-one match between the prediction and the masks at the sequence level.

A.7 Repeatability

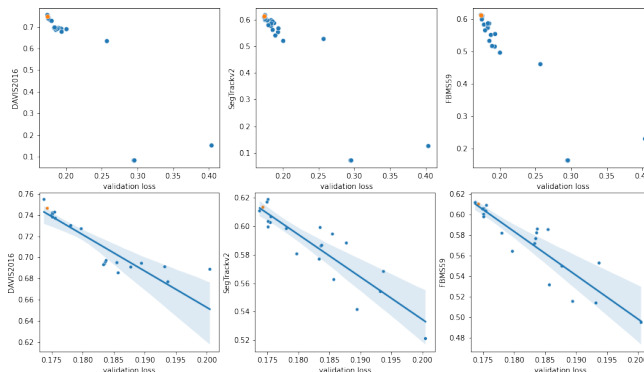


Figure 7: Model scores depending on initialization. Each dot represents a trained model. The x -axis represents the validation loss on the DAVIS 2016 train dataset, and the y -axis the performance on the evaluation dataset. The top row includes all models and the bottom row excludes models that diverged during training (validation loss > 0.25). The bottom row displays the linear relationship between validation loss and evaluation score. The model whose results are reported in the main text is represented as an orange dot.

With the introduction of the transformer decoder, we experimentally found that the convergence of the network depends on the weights initialization, and that the same network and loss configuration can yield different results at test time. In Fig.7, we show that our unsupervised loss on a held-out validation set is a good indicator of the network performance at test time. This is a critical point for model and hyperparameter selection, since we do not have access to the ground truth at training time (with our fully unsupervised scenario), and thus we cannot evaluate model performance. Fig.8 plots the model performance after training as a function of the initialization budget.

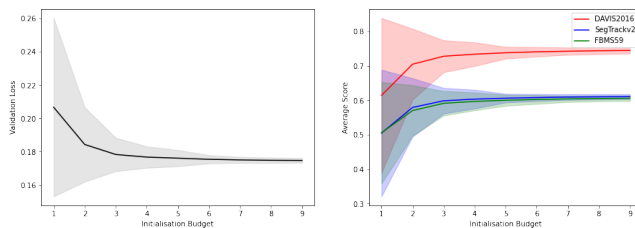


Figure 8: Evolution of the model performance as a function of the initialization budget. Left : the validation loss associated to the best network of each subset. Right : average performance on the test data set associated to this network for each different budget. The filled area correspond to +/- the standard deviation for each curve.

In our evaluation experiments, we account for this randomness by training five models with the same set of seeds for all ablations and by reporting the score of the model with the lowest validation loss for each model.

A.8 Training on real-world data

Table 5: Training on synthetic (FT3D) and on real (DAVIS2016) data

Training mode / Dataset	DAVIS2016		FBMS59		SegTrackv2	
	10	120	10	120	10	120
Full Model LT-MS-K4 (FT3D)	74.8	72.4	61.0	58.2	61.3	60.4
Full Model LT-MS-K4 (DAVIS2016)	73.6	72.8	60.0	57.6	62.8	61.3

We have trained our model LT-MS-K4 on the DAVIS2016 training set and evaluated it on DAVIS2016 validation set, FBMS59 and SegTrackV2. Results are collected in Table 5 and compared with those obtained when training our model on the synthetic FT3D dataset. We can observe that performance when training on DAVIS2016 remains globally on par with performance when training on FT3D. Let us note that the volume of data is much smaller when training on DAVIS 2016.

A.9 Influence of the cut size at inference

We have also tested how our LT-MS-K4 method behaves when varying the length of the input flow sequence. Results are plotted in Fig.10 for three datasets, DAVIS2016, FBMS59 and SegTrackV2. As expected, the best performance is obtained for the smallest length (equal to 10) of the input flow sequence. However, performance decreases slowly when the length increases, and remains stable for larger ones. It demonstrates the intrinsic ability of the LT-MS method to achieve accurate and consistent motion segmentation over long periods of the video, which is a unique property. We also did it for LT-MS-K2 as reported in Table 6. We even get slightly better results for DAVIS2016 and SegTrackV2 when the video sequence is processed in one go, i.e., with an infinite cutsize.

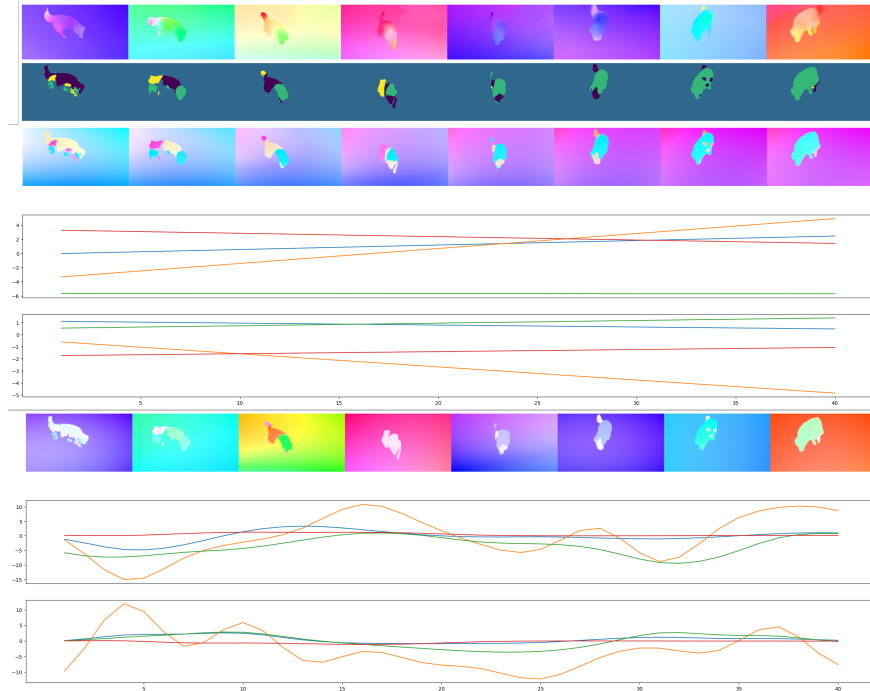


Figure 9: Visual assessment of the contribution of the spline-based motion model on the *dog* video of DAVIS2016 dataset (with $K = 4$). From top to bottom: input flows of the sequence; corresponding predicted motion segmentation maps; flows reconstructed with the space-time polynomial motion model; plots over time of the mean-value of the u -components of the flows provided per segment by the space-time polynomial motion models; plots over time of the mean-value of the v -components of the flows provided per segment by the space-time polynomial motion models; flows reconstructed with the space-time spline-based motion model; plots over time of the mean-value of the u -components of the flows provided per segment by the spline-based motion models; plots over time of the mean-value of the v -components of the flows provided per segment by the spline-based motion models. Clearly, the space-time polynomial model fails to handle non-uniformly varying motion, whereas the spline-based model does.

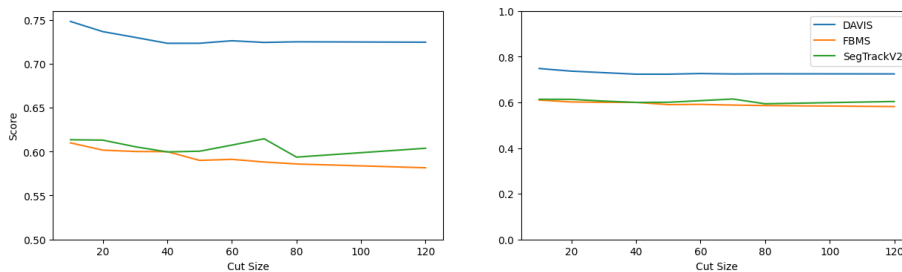


Figure 10: Influence of the length of the input flow sequence (also referred to as cut size on the horizontal axis of the plot) on the LT-MS-K4 method for three datasets, DAVIS2016, FBMS59 and SegTrackV2. As expected, the best performance is obtained for the smallest length (cut size equal to 10), but performance decreases slowly when the cut size increases and remains stable for larger ones. On the right, the plot is shown with the full range of values on the ordinate $[0, 100]$. On the left, a zoomed-in version of the plot.

Table 6: Results obtained on the three datasets DAVIS2016, FBMS59 and SegTrackV2 with LT-MS-K2 for respectively a cut size of 10 and no cut (the video sequence is processed in one go).

Dataset	DAVIS2016		FBMS59		SegTrackV2	
	10	∞	10	∞	10	∞
LT-MS-K2	70.3	70.7	55.3	48.7	58.6	59.3

A.10 Additional visual evaluation

Additional visual results of our LT-MS method are provided in Fig.11. We can observe that the motion segments are globally accurate. Let us recall that the ground-truth is not necessarily available for all the video frames depending on the datasets. Since our method involves several masks, we can properly handle articulated motions (*monkey*), deal with the presence of several moving objects in the scene (*hummingbird*), or accomodate motion parallax (*libby*).

In Fig.12, we collect additional visual results on three videos of the SegTrackV2 dataset, from top to bottom, the *birdfall*, *bird-of-paradise*, and *bmX* videos. Results demonstrate the ability of our long-term segmentation method to recover, to some extent, correct segmentation even from flow fields wrongly computed at some time instants.

References

- [1] D.P. Kingma and M. Welling. An introduction to variational autoencoders. *Foundations and Trends in Machine Learning*, 12(4):307-392, 2019.
- [2] D. Lao, Z. Hu, F. Locatello, Y. Yang, and S. Soatto. Divided attention: Unsupervised multi-object discovery with contextually separated slots. *arXiv:2304.01430*, April 2023.
- [3] D. Liu and J. Nocedal. On the limited memory BFGS method for large scale optimization. In *Mathematical Programming*, 45(1-3):503-528, 1989.

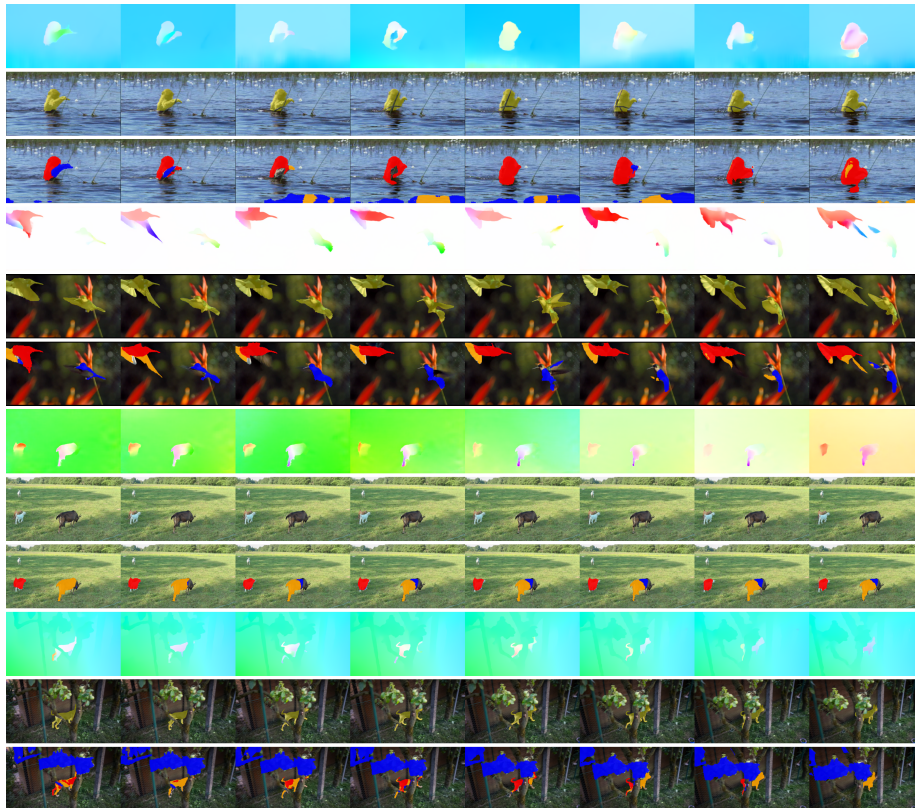


Figure 11: Results obtained with our LT-MS-K4 method ($K = 4$). Four groups of results are displayed: *monkey*, *hummingbird* from SegTrackV2, *goats01* from FBMS59 and *libby* from DAVIS2016. For each group, the first row samples successive flow fields (HSV color code) corresponding to the processed video. The second row contains the corresponding images of the video, where the ground-truth of the moving object is overlaid in yellow (when available at that frame). The third row shows the motion segments provided by our LT-MS-K4 method with one colour per segment. For all the results, we adopt the same color set for the three masks corresponding to the moving objects (blue, red and orange), and we let the background image for the background mask.

- [4] E. Meunier and P. Bouthemy. Unsupervised space-time network for temporally-consistent segmentation of multiple motions. In *Conference on Computer Vision and Pattern Recognition (CVPR)*, Vancouver, June 2023.
- [5] J. Xie, W. Xie, and A. Zisserman. Segmenting moving objects via an object-centric layered representation. In *Conference on Neural Information Processing Systems (NeurIPS)*, 2022.

A.11 Detailed results per videos of the datasets

Hereafter, we report detailed results through tables collecting the evaluation scores obtained by our LT-MS-K4 method for every video of the two datasets DAVIS2016 and Seg-TrackV2 (binary evaluation), and by our LT-MS-K3 model for every video of the DAVIS2017-motion dataset and FBMS59 (multi-mask evaluation). Let us recall that the official evaluation algorithm is not the

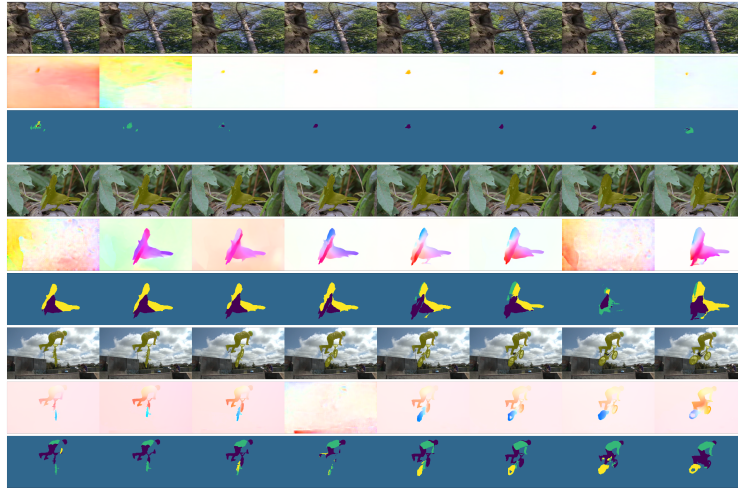


Figure 12: Illustration of the temporal consistency provided by our LT-MS-K4 method for three examples, the *birdfall*, *bird-of-paradise*, and *bmx* videos of SegTrackV2. For each group, the first row contains the video images with the ground truth overlaid in yellow when available; the second row depicts the corresponding flow fields represented with the HSV code while normalized independently from each other; the third row provides the predicted segmentation.

same for DAVIS2016 and DAVIS2017-motion. The evaluation is done on the whole video for DAVIS2017-motion and is multi-segment, while it is binary and performed frame by frame of the video for DAVIS2016.

A.11.1 DAVIS2016

A.11.2 SegTrackV2

A.11.3 DAVIS2017-motion

A.11.4 FBMS59 - Multiple Masks

Video	\mathcal{J} (M)	\mathcal{J} (O)	\mathcal{J} (D)	\mathcal{F} (M)	\mathcal{F} (O)	\mathcal{F} (D)
blackswan	0.515	0.521	-0.091	0.561	0.833	-0.036
bmw-trees	0.596	0.744	0.234	0.795	0.923	0.125
breakdance	0.740	1.000	0.038	0.722	1.000	0.000
camel	0.867	1.000	0.104	0.858	1.000	0.101
car-roundabout	0.920	1.000	-0.004	0.806	1.000	-0.060
car-shadow	0.901	1.000	0.011	0.848	1.000	-0.017
cows	0.872	1.000	0.026	0.798	1.000	0.009
dance-twirl	0.821	1.000	-0.113	0.842	1.000	-0.045
dog	0.769	1.000	-0.085	0.671	1.000	-0.076
drift-chicane	0.718	0.860	0.063	0.793	0.860	0.161
drift-straight	0.892	1.000	0.047	0.838	1.000	0.229
goat	0.380	0.330	-0.087	0.367	0.114	-0.069
horsejump-high	0.843	1.000	0.064	0.896	1.000	-0.002
kite-surf	0.518	0.500	0.114	0.494	0.375	-0.035
libby	0.781	1.000	0.108	0.892	1.000	0.035
motocross-jump	0.750	0.842	0.042	0.590	0.658	0.092
paragliding-launch	0.621	0.667	0.299	0.308	0.179	0.357
parkour	0.711	0.878	-0.315	0.765	0.949	-0.157
scooter-black	0.854	1.000	-0.036	0.729	1.000	0.072
soapbox	0.891	1.000	0.020	0.863	1.000	0.020
Average	0.748	0.867	0.022	0.722	0.845	0.035

Table 7: Results given for every video of DAVIS2016 dataset. Reported scores per video are the average Jaccard score over frames in the video. The very last row is the average over videos scores. \mathcal{J} is the Jaccard index and \mathcal{F} is the Countour Accuracy. The Mean (M) is the average of the scores, the Recall (O) is the fraction of frames per video with a score higher than 0.5, and the Decay (D) is the degradation of the score over time in the video.

Video	Jacc (\mathcal{J})
bird of paradise	0.596
birdfall	0.468
bmw	0.776
cheetah	0.438
drift	0.431
frog	0.792
girl	0.651
hummingbird	0.697
monkey	0.607
monkeydog	0.241
parachute	0.928
penguin	0.517
soldier	0.752
worm	0.514

Table 8: Results given for every video of SegTrackV2 dataset. Each reported score is the average Jaccard score over annotated frames in the video. The very last row is the average over all the frames and over all the videos.

Sequence	J-Mean	F-Mean
bike-packing`1	0.078	0.327
bike-packing`2	0.254	0.267
blackswan`1	0.477	0.575
bmx-trees`1	0.608	0.804
breakdance`1	0.450	0.526
camel`1	0.772	0.726
car-roundabout`1	0.913	0.810
car-shadow`1	0.896	0.845
cows`1	0.821	0.728
dance-twirl`1	0.444	0.576
dog`1	0.654	0.571
dogs-jump`1	0.019	0.147
dogs-jump`2	0.254	0.323
dogs-jump`3	0.303	0.351
drift-chicane`1	0.557	0.627
drift-straight`1	0.886	0.829
goat`1	0.220	0.300
gold-fish`1	0.018	0.240
gold-fish`2	0.282	0.336
gold-fish`3	0.357	0.356
gold-fish`4	0.000	0.000
gold-fish`5	0.000	0.000
horsejump-high`1	0.721	0.794
india`1	0.066	0.085
india`2	0.163	0.172
india`3	0.072	0.108
judo`1	0.225	0.397
judo`2	0.286	0.414
kite-surf`1	0.449	0.464
lab-coat`1	0.332	0.350
libby`1	0.746	0.853
loading`1	0.057	0.246
loading`2	0.128	0.259
loading`3	0.427	0.514
mbike-trick`1	0.444	0.436
motocross-jump`1	0.446	0.435
paragliding-launch`1	0.577	0.286
parkour`1	0.531	0.646
pigs`1	0.105	0.433
pigs`2	0.437	0.431
pigs`3	0.059	0.217
scooter-black`1	0.843	0.724
shooting`1	0.434	0.568
soapbox`1	0.487	0.696

Table 9: Results given for every video of D17 dataset.

J&FMean	JMean	JRecall	JDecay	FMean	FRecall	FDecay
0.422	0.393	0.387	0.004	0.450	0.437	0.024

Table 10: Results given for every video of DAVIS2017-motion dataset. The very last row is the average score over all the videos for the different criteria.

Video	bIoU (\mathcal{J})	Linear Assignment Sequence (\mathcal{J})
camel01	0.599	0.591
cars1	0.698	0.527
cars10	0.484	0.324
cars4	0.78	0.561
cars5	0.578	0.515
cats01	0.76	0.76
cats03	0.698	0.492
cats06	0.469	0.393
dogs01	0.814	0.814
dogs02	0.766	0.434
farm01	0.613	0.519
giraffes01	0.502	0.446
goats01	0.424	0.336
horses02	0.549	0.436
horses04	0.458	0.366
horses05	0.327	0.145
lion01	0.426	0.376
marple12	0.386	0.324
marple2	0.501	0.291
marple4	0.945	0.945
marple6	0.446	0.311
marple7	0.643	0.44
marple9	0.384	0.231
people03	0.406	0.298
people1	0.892	0.892
people2	0.741	0.616
rabbits02	0.507	0.445
rabbits03	0.578	0.514
rabbits04	0.615	0.444
tennis	0.519	0.382
Seq Average	0.584	0.472

Table 11: Results given for every video of FBMS59 dataset. Each reported score is the average Jaccard score over annotated frames in the video. The very last row is the average of the score over videos.